ELSEVIER

Journal of Crystal Growth 208 (2000) 327–340

JOURNAL OF CRYSTAL GROWTH

www.elsevier.nl/locate/jcrysgro

Three-dimensional simulation of vertical zone-melting crystal growth: symmetry breaking to multiple states

C.W. Lan*, M.C. Liang

Chemical Engineering Department, National Taiwan University, Taipei 10617, Taiwan, ROC

Received 20 April 1999; accepted 16 August 1999
Communicated by D.T.J. Hurle

Abstract

For the first time three dimensional simulation is conducted for vertical zone-melting crystal growth, simultaneously considering the time-dependent fluid flow, heat transfer, and moving interfaces. The numerical method is based on an efficient finite-volume method with front tracking. The growth of 2-cm diameter GaAs in a quartz ampoule is used as an example. Under an axisymmetric operation, the two-dimensional solution can bifurcate subcritically to three-dimensional ones as the convection or superheating increases. The three-dimensional modes, which can have either one- or two-fold symmetry, depend on the equilibrium aspect ratio of the molten zone. Under normal gravity, the axisymmeric mode exists only for low superheating. Furthermore, the multiple states, including other multi-fold modes, are path dependent, which are further illustrated though the dynamics of heating and cooling operations. © 2000 Elsevier Science B.V. All rights reserved.

PACS: 44.25. + f; 47.27.Te; 81.10.Fq; 02.60.Cb; 02.70.Fj

Keywords: 3D simulation; Zone-melting; Bifurcation; Interface; Buoyancy convection; Multiple states; Dynamics

1. Introduction

The vertical zone-melting (VZM) crystal growth is an important process for both crystal growth and purification [1–4]. There are several advantages of using such a technique for crystal growth. In addition to in situ purification, the convex growth front can be easily obtained by adjusting the zone length. The zone-leveling of the dopant also minimizes the axial segregation. However, because of the radial zone heating, the thermal convection induced is strong, and the growth interface can be significantly affected [5,6]. To understand the role of heat flow on the growth, numerical simulation is usually adopted, and it has been proved useful in growth control, especially in the control of the zone shape and segregation [7]. However, the complexity of the process is introduced not only by the stronger convection, but also by nonlinear bifurcations, both the multiplicity and the unsteadiness. The most typical bifurcation for VZM is symmetry breaking, which is the transition from an axisymmetric mode to three-dimensional (3D) ones. As the bifurcation is encountered, in addition to the

---

* Corresponding author. Fax: + 886-2-23633917.
E-mail address: lan@ruby.che.ntu.edu.tw (C.W. Lan)

PII: S0022-0248(99)00455-8

dramatic changes of the heat flow, mixing, and the growth interface, the operational uncertainty during crystal growth is one of the key issues. It is particularly important if the bifurcation is subcritical which may cause catastrophic runaway during a steady growth. Unfortunately, very little study has been devoted to this subject [8,9].

There are several two-dimensional (2D) models being developed for VZM crystal growth (e.g., Refs. [5–8]). Time-dependent calculations including fluid flow, heat and mass transfer, and the moving interfaces have also been conducted recently [7,8]. Although the 2D models give useful information on the growth control and design, they are still not adequate. Very often, 3D flows and heat transfer can be induced as the driving force for convection, which is often characterized by the Rayleigh number ($\mathrm{Ra_T}$), large enough, even though the system arrangement and the heating are perfectly axisymmetric [9]. Neumann [10] and Baumgartl et al. [11] showed that the symmetry breaking occurred supercritically from an axisymmetric mode (the so-called *m*0 mode) to a 3D one-fold mode (*m*1 mode). Time-dependent flows were also observed at higher $\mathrm{Ra_T}$. However, their studies were based on an over-simplified model, where the deformable interfaces and the ampoule were ignored. A parabolic temperature profile was imposed at the melt surface. The bifurcation structure of the problem was not clear as well. In fact, it is believed that the interfaces can have significant effects on the stability and the bifurcation structure during solidification, and several examples have been illustrated [12,13]. In reality, the zone shape as well as the zone length also changes with the heating power and other thermal conditions. To model the system in a self-consistent manner, a full 3D model including the free interfaces and the ampoule is necessary. Unfortunately, no such model for VZM has been reported.

In the present study, a finite volume method (FVM) with a front tracking technique is developed to study the bifurcation and dynamics of the VZM growth of 2-cm GaAs in a quartz ampoule. In addition to the primary bifurcation from the modes *m*0 to *m*1 or *m*2 (two-fold symmetry), secondary bifurcation from *m*2 to *m*1 will be illustrated. Some interesting transition during heating and cooling are further discussed. Although inherent time-dependent flows are also important, we will not pay much attention to them in this report. We shall discuss them elsewhere. In the next section, the mathematical model and numerical solution are described. Section 3 is devoted to results and discussion, where detailed benchmark comparison will be performed. Brief conclusions are drawn in Section 4.

2. Model description and numerical solution

A generic VZM crystal growth system is illustrated in Fig. 1(a). Since axisymmetry is no longer assumed here, the system is described by a Cartesian coordinate (x, y, z). The zone heater is described by an effective heating profile $T_a(z,t)$, which is kept axisymmetric in this study. The ampoule pulling speed U_{amp} and the heater moving speed U_{h} can be given independently. The flow and temperature fields as well as the melt/feed ($h_{\mathrm{f}}(x,y,z,t)$) and melt/crystal ($h_{\mathrm{c}}(x,y,z,t)$) interfaces are also represented in the Cartesian coordinate.

The dimensionless variables are defined by scaling length with the crystal diameter D_{c}, time with $D_{\mathrm{c}}^2/\alpha_{\mathrm{m}}$, velocity with $\alpha_{\mathrm{m}}/D_{\mathrm{c}}$, pressure with $\rho_{\mathrm{m}}\alpha_{\mathrm{m}}^2/D_{\mathrm{c}}^2$, and temperature with the melting point T_{m}, where α_{m} is the thermal diffusivity and ρ_{m} the melt density. The time-dependent governing equations describing the convection and heat transport in the melt (m) are as follows:

$$\nabla \cdot \boldsymbol{v} = 0, \tag{1}$$

$$\partial \boldsymbol{v}/\partial \tau + \boldsymbol{v} \cdot \nabla \boldsymbol{v} = -\nabla P + \mathrm{Pr}\nabla^2 \boldsymbol{v} - \mathrm{Pr}\mathrm{Ra_T}(\theta - 1)\boldsymbol{e}_{\mathrm{g}}, \tag{2}$$

$$\partial \theta/\partial \tau + \boldsymbol{v} \cdot \nabla \theta = \nabla^2 \theta, \tag{3}$$

where τ, $\boldsymbol{v}$, P, and θ are the dimensionless time, velocity, pressure, and temperature, respectively. Pr is the Prandtl number. The gravity direction $\boldsymbol{e}_{\mathrm{g}}$ the unit vector of gravity, which is aligned with the growth axis in this study. T_{m} also serves as a reference temperature. The associated dimensionless number $\mathrm{Ra_T}$ in the source term of the momentum equation is the thermal Rayleigh number,

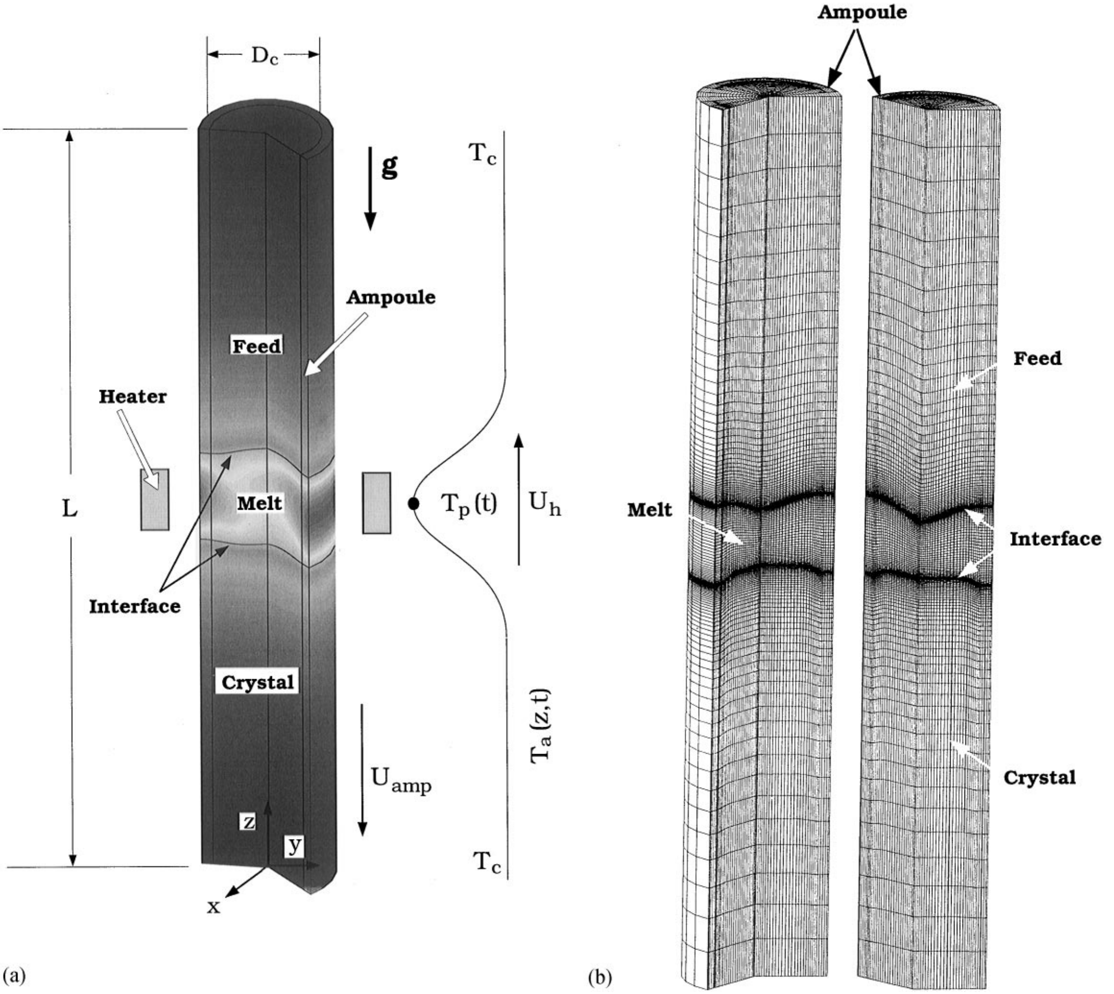

Fig. 1. (a) Schematic sketch of vertical zone-melting (VZM) crystal growth; (b) a sample mesh for calculation using finite volume method.

defined as follows:

$$\mathrm{Ra_T} \equiv \frac{g\beta_{\mathrm{T}} T_{\mathrm{m}} D_{\mathrm{c}}^3}{\alpha_{\mathrm{m}} \nu_{\mathrm{m}}},$$

where g is the gravitational acceleration, β_{T} the thermal expansion coefficients, and ν_{m} is the kinematic viscosity.

In the crystal (c), the feed (f), and the ampoule (a), only heat transfer needs to be considered:

$$\partial\theta/\partial\tau - v_{\mathrm{amp}}\boldsymbol{e}_z \cdot \nabla\theta = \tilde{\kappa}_i \nabla^2\theta,\ (i = \mathrm{c, f, a}), \tag{4}$$

where $\tilde{\kappa} \equiv \alpha_i/\alpha_{\mathrm{m}}$ is the dimensionless thermal diffusivity of feed, crystal or ampoule; α_i is the thermal diffusivity of the feed ($i = \mathrm{f}$) or the crystal ($i = \mathrm{c}$).

The no-slip condition is used for the velocity on solid boundaries:

$$\boldsymbol{v} = -\gamma_c v_{\mathrm{amp}} \boldsymbol{e}_z, \tag{5}$$

where $\gamma_{\mathrm{c}} \equiv \rho_{\mathrm{c}}/\rho_{\mathrm{m}}$ and v_{amp} is the dimensionless ampoule pulling speed.

The thermal boundary conditions at the melt/solid interfaces are set by the heat flux balances:

$$\boldsymbol{n}\cdot\nabla\theta|_{\mathrm{m}} - \boldsymbol{n}\cdot\kappa_{\mathrm{c}}\nabla\theta|_{\mathrm{c}} + (v_{\mathrm{amp}} + \mathrm{d}h_{\mathrm{c}}/\mathrm{d}\tau)\mathrm{St}(\boldsymbol{n}\cdot\boldsymbol{e}_z) = 0, \quad (6)$$

$$\boldsymbol{n}\cdot\nabla\theta|_{m} - \boldsymbol{n}\cdot\kappa_{\mathrm{f}}\nabla\theta|_{\mathrm{f}} + (v_{\mathrm{amp}} + \mathrm{d}h_{\mathrm{f}}/\mathrm{d}\tau)\mathrm{St}(\boldsymbol{n}\cdot\boldsymbol{e}_z) = 0, \quad (7)$$

where $\boldsymbol{n}$ is the unit normal vector at the feed or growth interfaces pointing to the melt and $\kappa_i \equiv k_i/k_m$ the ratio of the thermal conductivity of phase i to the melt ($i = \mathrm{f, c}$); k_{m} is the thermal conductivity of the melt. The Stefan number $\mathrm{St} \equiv \Delta H/Cp_{\mathrm{m}}T_{\mathrm{m}}$ scales the heat of fusion (ΔH) released during solidification to the sensible heat in the melt; Cp_{m} is the specific heat of the melt.

The heat exchange between the ampoule and the furnace is by both radiation and convection according to the energy balance along the ampoule surface,

$$-\boldsymbol{n}\cdot\kappa_{\mathrm{a}}\nabla\theta|_{\mathrm{a}} = \mathrm{Bi}(\theta - \theta_{\mathrm{a}}) + \mathrm{Rad}(\theta^4 - \theta_{\mathrm{a}}^4), \quad (8)$$

where $\boldsymbol{n}$ is the unit normal vector on the ampoule surface pointing outwards, $\mathrm{Bi} \equiv hD_{\mathrm{c}}/k_{\mathrm{m}}$ the Biot number, and $\mathrm{Rad} \equiv \sigma\varepsilon_{\mathrm{a}}T_{\mathrm{m}}^3D_{\mathrm{c}}/k_{\mathrm{m}}$ the Radiation number; σ is the Stefan Boltzmann constant, while ε_{a} is the surface emissivity of the ampoule. For simplicity, the effective heater temperature θ_{a} is assumed to be a Gaussian distribution:

$$\theta_{\mathrm{a}}(z,t) = \theta_{\mathrm{a}\infty} + (\theta_{\mathrm{p}} - \theta_{\mathrm{a}\infty})\exp(-[(z - z_{\mathrm{p}})/\mathrm{a}]^2), \quad (9)$$

where, $\theta_{\mathrm{a}\infty}$ and θ_{p} are the dimensionless ambient background and peak temperatures, respectively, and a is related to the width of distribution. In the present study, all the boundary and heating conditions are axisymmetric.

The above governing equations and their associated boundary conditions can only be solved numerically. We have developed efficient FVM schemes using the primitive variable formulation [14] and multigrid acceleration [15] for the free or moving boundary problem. For time-dependent calculations, a fully implicit Euler scheme [16] is used for the time-derivative terms. A sample converged mesh for calculation is shown in Fig. 1(b). As shown, finer grid spacing is placed near the interfaces to enhance the accuracy of calculation. Detailed description of the numerical method can be found elsewhere [14,15].

3. Results and discussion

Before presenting the results, we have performed extensive benchmark comparisons with previous works for both a simplified 3D model and a full 2D model. For the simplified 3D model, the feed and growth fronts are assumed flat and fixed. The ampoule is also removed, while a parabolic temperature profile is specified along the melt surface. For $\mathrm{Ra}_{\mathrm{T}}^{\ddagger} = 2\times10^5$, we have obtained a pseudo-steady 3D solution, as shown in Fig. 2(a), where the axisymmetric solution is not possible. For comparison purposes, in this case the definition of the Rayleigh number is somewhat different, i.e., $\mathrm{Ra}_{\mathrm{T}}^{\ddagger} \equiv (2g\beta_{\mathrm{T}}(T_{\mathrm{max}} - T_{\mathrm{m}})D_{\mathrm{c}}^3)/\alpha_{\mathrm{m}}v_{\mathrm{m}}$, where the maximum temperature difference ($T_{\mathrm{max}} - T_{\mathrm{m}}$) is used. As shown, our result is in good agreement with that obtained by Baumgartl et al. [11] and by a commercial CFD code, Fluent [17]. Good agreement with the Fluent's result is also obtained for $\mathrm{Ra}_{\mathrm{T}}^{\ddagger} = 4\times10^5$, as shown in Fig. 2(b). However, for both cases, the calculated results are not stable. Time-dependent calculations are further performed for both cases with finite disturbances using our code and Fluent, but the oscillations are not regular. Time-dependent results are found for $\mathrm{Ra}_{\mathrm{T}}^{\ddagger} > 35{,}000$ for the asymmetric $m0$ mode and $\mathrm{Ra}_{\mathrm{T}}^{\ddagger} > 2\times10^5$ for the $m1$ mode, which agree reasonable well with previous calculations [11]. It should be pointed out that the Hopf bifurcation, where the flow starts to oscillate, strongly depends on the thermal boundary conditions. Therefore, the onset of the unsteadiness at $\mathrm{Ra}_{\mathrm{T}}^{\ddagger} = 35{,}000$ is not universal.

The comparison with the full 2D model [7,8], which uses the stream function/vorticity formulation, is possible if the axisymmetric solution is stable. Therefore, calculations are then performed for both high ($T_{\mathrm{p}} = 1600°\mathrm{C}$) and low superheatings ($T_{\mathrm{p}} = 1500°\mathrm{C}$). However, for high superheating, the axisymmetric solution exists only for low gravity. For example, at 0.1 g, we obtain an axisymmetric solution, as shown in Fig. 3(a); $\mathrm{Ra}_{\mathrm{T}}^{\ddagger} \approx 9\times10^4$. As shown, the result is in good agreement with the 2D one for both the interface shapes and isotherms.

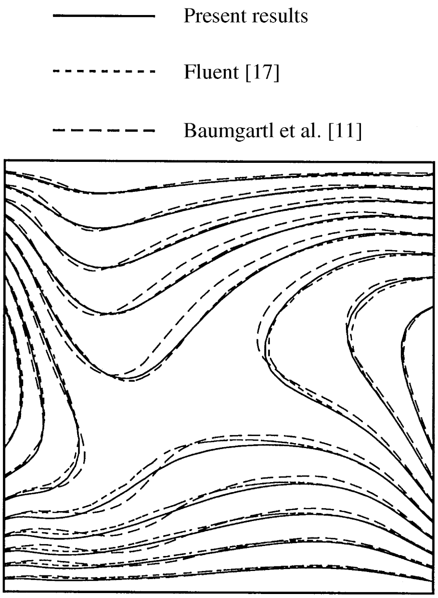

$\mathrm{Ra}^*_\mathrm{T} = 200{,}000$

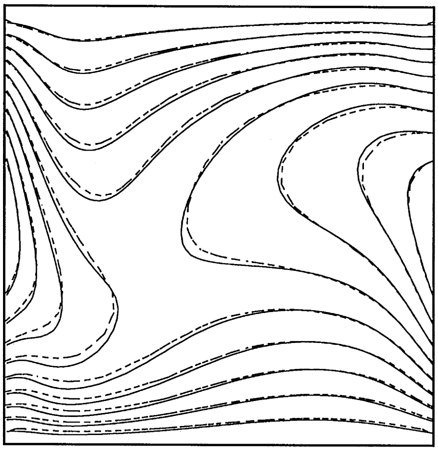

$\mathrm{Ra}^*_\mathrm{T} = 400{,}000$

Fig. 2. Comparison of the simplified 3D model (a) $\mathrm{Ra}_\mathrm{T} = 2\times10^5$; (b) $\mathrm{Ra}^*_\mathrm{T} = 4\times10^5$.

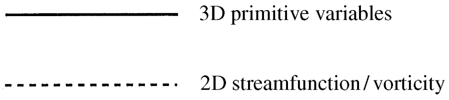

(a) High super-heating

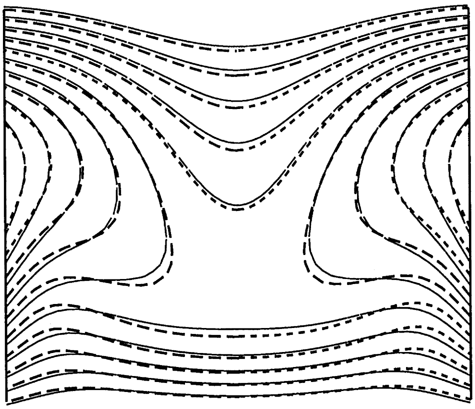

Zone length = 1.49 cm (3D)
1.48 cm (2D)

Overheating = 97.11°C (3D)
96.75°C (2D)

(b) Low super-heating

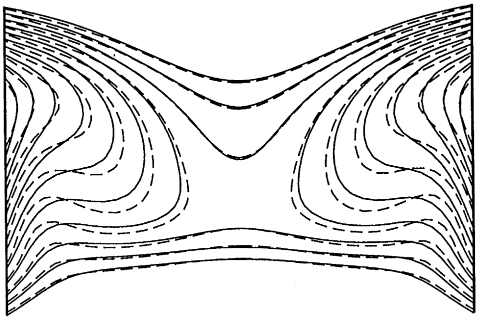

Zone length = 0.758 cm (3D)
0.749 cm (2D)

Overheating = 41.79°C (3D)
41.08°C (2D)

Fig. 3. Comparison of the 2D full model: (a) high superheating (0.1 g); (b) low superheating (normal gravity).

For the convenience of illustration, the ampoule is not shown here. However, one may use Fig. 1(a) to get a whole picture of simulation.

For lower superheating ($\mathrm{Ra}^*_\mathrm{T} \approx 4.5\times10^5$), an axisymmetric solutions can be stable under normal gravity. Again, the axisymmetric solution we obtained is compared with the 2D result. As shown in Fig. 3(b), again, the agreement is reasonably good. Due to the lower superheating in the melt, the discrepancy seems to be slightly larger than the previous one. Nevertheless, from numerical

Table 1
Physical properties and some input parameters [9]

GaAs
$\rho_c = \rho_f = 5.7\ \mathrm{g\ cm^{-3}}$
$\rho_m = 5.7\ \mathrm{g\ cm^{-3}}$
$T_m = 1238°\mathrm{C}$
$\Delta H = 726\ \mathrm{J\ g^{-1}}$
$h = 1.6 \times 10^{-2}\ \mathrm{W\ cm^{-2}\ °C^{-1}}$
$k_c = k_f = 0.07\ \mathrm{W\ cm^{-1}\ °C^{-1}}$
$k_m = 0.14\ \mathrm{W\ cm^{-1}\ °C^{-1}}$
$Cp_c = Cp_f = Cp_m = 0.42\ \mathrm{J\ g^{-1}\ °C^{-1}}$
$\beta_T = 1.16 \times 10^{-4}\ \mathrm{K^{-1}}$
Quartz (ampoule)
$\rho_a = 2.2\ \mathrm{g\ cm^{-3}}$
$k_a = 0.035\ \mathrm{W\ cm^{-1}\ °C^{-1}}$
$Cp_a = 0.188\ \mathrm{J\ g^{-1}\ °C^{-1}}$
$\varepsilon_a = 0.8$
Other input parameters
$L = 15$ cm
$D_c = 2$ cm
$D_a = 2.4$ cm
$T_p = 1600°\mathrm{C}$ (for high superheating); 1500°C (for low superheating).
$T_{a\infty} = 300°\mathrm{C}$
$a_f = a_c = 1.8$ cm (for high superheating); 2.0 cm (for low superheating)
$z_{p0} = 7.5$ cm
$U_h = 0$ cm/h (for fully transient calculations)
Dimensionless groups
$\mathrm{Pr} = 0.059$; $\mathrm{Ra_T} = g\beta_T T_m D_c^3/(\alpha_m \nu_m) = 0 \sim 6.9 \times 10^6$;
$\mathrm{Ra_T^*} = 2g\beta_T \Delta T D_c^3/(\alpha_m \nu_m) = 0 \sim 9.133 \times 10^5$ (for $\Delta T = T_{max} - T_m = 100°\mathrm{C}$)

simulation point of view, both codes give consistent results, even though their formulations and code implementation are very different.

For numerical simulation, the mesh may also affect the result. To balance CPU time and accuracy, we have adopted the mesh similar to Fig. 1(b) for all calculations here. Such a mesh ($34 \times 24 \times 146$ finite volumes, in the r, θ, and z directions, respectively) leads to 223,968 equations. In this study, all computations are performed in an HP/C180 workstation or a Pentium II/450MHz PC, and one steady-state calculation takes about 2 h of CPU time.

After building the confidence through the code verification, we are ready to study the process in detail. Following the results from the previous 2D benchmarks, in the following sections, we will construct the bifurcation diagrams for both examples to illustrate their symmetric breaking and possible multiple states. The physical properties and input parameters used in the computation are listed in Table 1.

3.1. High superheating — effects of convection

The first case is conducted for the high superheating at $T_p = 1600°\mathrm{C}$; the superheating in the melt is about 100°C for 0 g and about 80°C for 1 g. The high superheating condition is generated through a sharper heating profile (with a smaller a and a larger T_p). As mentioned for Fig. 2(a), with such a high superheating, the axisymmetric solution is not possible at normal gravity. Therefore, to illustrate the loss of axisymmetry (or symmetry breaking), solution tracking is performed by using the gravity as the continuation parameter. Also, to better examine symmetry breaking, the zone length difference and the maximum surface temperature difference (at the melt/ampoule interface) are adopted. These values are zero if the axisymmetry is retained. The bifurcation diagram using the zone length difference as a function of gravity is shown in Fig. 4(a), while using the temperature difference is shown in Fig. 4(b). As shown, both figures show a typical subcritical bifurcation from the 2D axisymmetric mode (*m*0) to the 3D *m*1 mode. In this case, the 2D result can be obtained only for smaller *g* or weaker convection (up to 0.18 g). As the flow becomes 3D, significant nonuniformity in the zone length and the surface temperature appears. As shown in Fig. 4(a), the maximum zone length difference is up to 2 mm. Meanwhile, the temperature difference is up to 22°C in Fig. 4(b). After the maximum temperature difference reaches its maximum value, it decreases with the increasing gravity level due to the better heat transfer in the zone.

There is a range of gravity where multiple solutions exist. For example, at 0.1 g, both solutions a and b are stable, as illustrated in Fig. 5(a) and (b), respectively. The solution in Fig. 5(a) is axisymmetric, which is the same as the one shown in Fig. 3(a) for the comparison with the result obtained by the 2D stream function/vorticity model. For the 3D solution in Fig. 5(b), the isotherms and velocity fields at different planes are shown. For the 3D

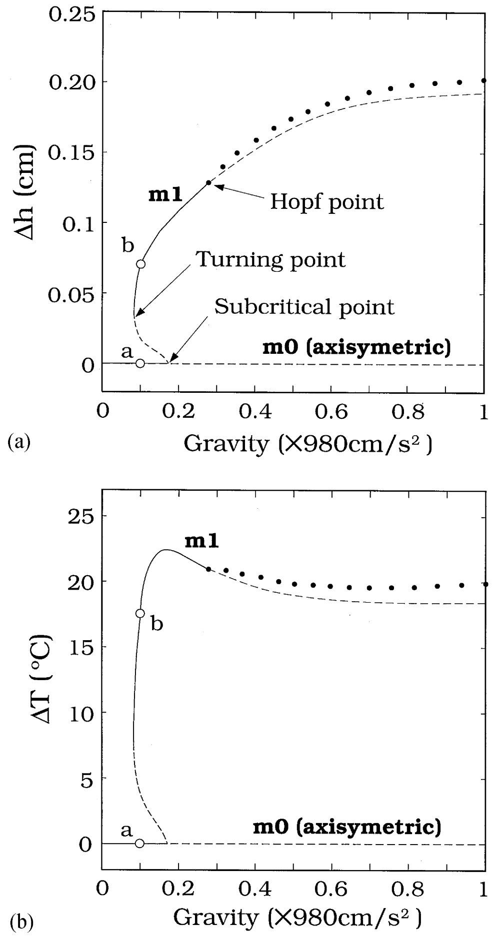

Fig. 4. Bifurcation diagrams of high superheating using the gravity level as the parameter: (a) zone length deviation; (b) surface temperature deviation. The black dots (●) indicate the maximum values of oscillations.

flow, an easy way to examine its symmetry is from the field plot at the plane of $z = L/2$, as shown on the upper right of Fig. 5(b). As shown, the minimum temperature moves to the left. Also, two flow cells can be seen. One major flow roll is developed in the lower left field plot. During simulation, we have no control of the direction for the 3D flow to develop. Therefore, after the result is obtained, we have to examine the mid-plane isotherms in order to decide which plane to illustrate the result, as the example shown in the bottom of Fig. 5(b). Furthermore, because the flow in the $m1$ mode is less restricted, as compared with $m0$, its convection is stronger. Heat transfer is enhanced slightly as well. This can be further illustrated by the normalized heat flux at the growth interface (based on the conduction mode at $0g$). This value is 1.1355 for the $m0$ mode and 1.1364 for the $m1$ mode. Interestingly, beside the most asymmetric plane, the plane with symmetric thermal and velocity fields, shown on the lower right of Fig. 5(b), is quite similar to the 2D solution in Fig. 5(a).

The subcritical nature of the bifurcation shown in Fig. 4 is particularly important in practice. One can imagine that as the operation condition passes the subcritical point (at about 0.18 g), a dramatic change in the flow and heat transfer may occur, because the stable $m1$ solution (say at 0.18 g) is quite far away from the unstable symmetric mode $m0$. On the other hand, as the driving force is reduced (decreasing g or Ra_T) from the top branch, a sudden loss of the $m1$ mode occurs at the turning point as well (at about 0.08 g). Such an uncertainty appears physically and thus makes the control of the process difficult. Furthermore, as g or Ra_T is further increased, we also find a Hopf point, where the flow starts to oscillate, at about 0.26 g ($\mathrm{Ra}_\mathrm{T}^{\ddagger} = 2.23 \times 10^5$). The oscillation of the zone length has a period of 450 s at 0.3 g; the period decreases to 88 s at 1 g ($\mathrm{Ra}_\mathrm{T}^{\ddagger} = 7.36 \times 10^5$). Interestingly, the Hopf point for this case is only slightly larger than the previous reported value (about 1.9×10^5) [11] using a simplified model. On the other hand, we have examined a similar fixed zone [18] using an uniform ambient temperature at 1711–1911 K by Fluent, where the heat transfer is from convection and radiation. Interestingly, the flow is stable up to $\mathrm{Ra}_\mathrm{T}^{\ddagger} = 9 \times 10^5$. Clearly, the Hopf point strongly depends on the thermal boundary conditions for this case.

3.2. Low superheating — effects of heater temperature

In practice, the superheating in the melt can be controlled by the heater. As shown previously, under normal gravity, the 2D axisymmetric mode can be stable only for low superheating (for example at $T_\mathrm{p} = 1500°\mathrm{C}$ for Fig. 3(b)). Therefore, it is thus worthwhile to continue studying this case (about 42°C superheating or $\mathrm{Ra}_\mathrm{T}^{\ddagger} = 3.84 \times 10^5$) for normal

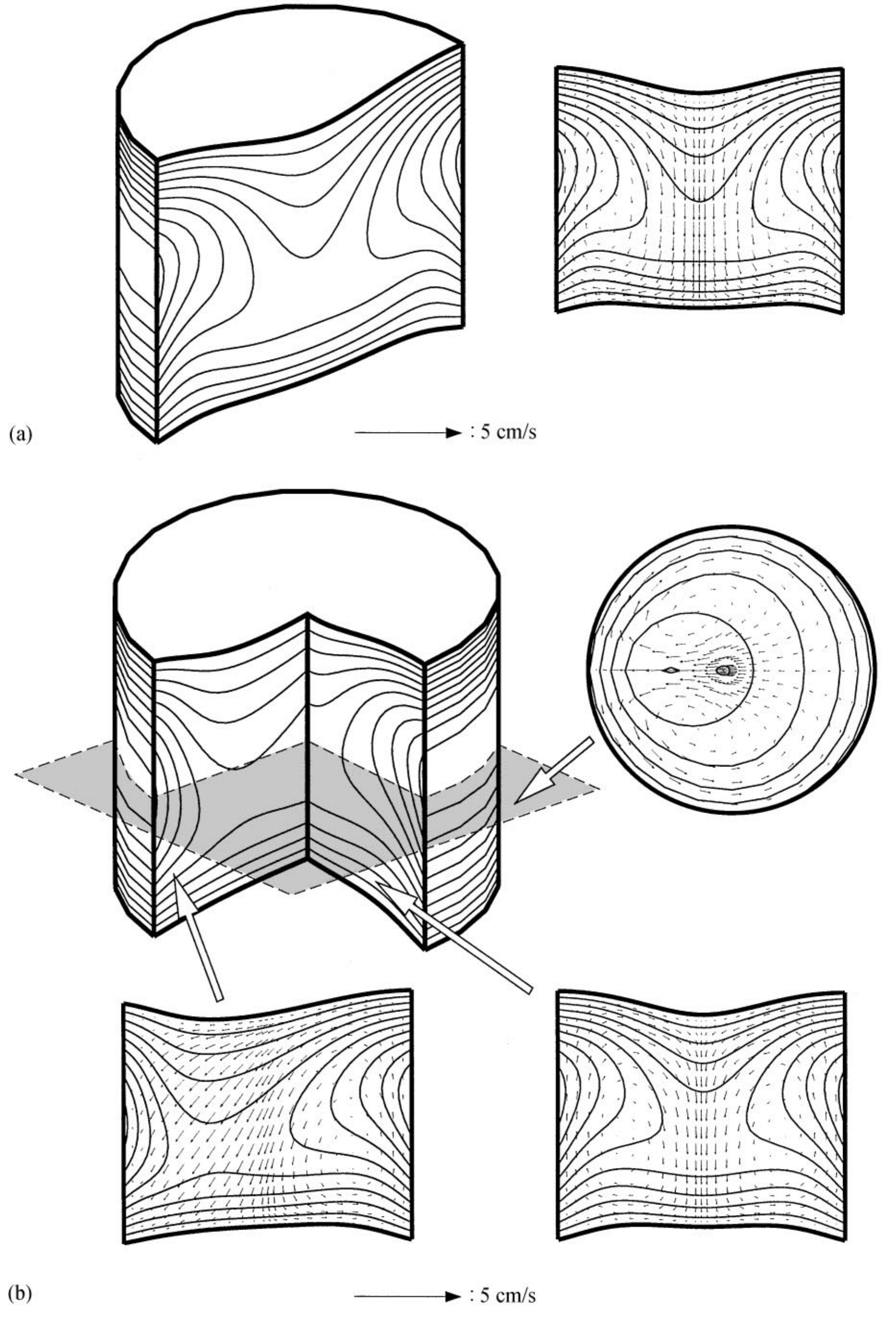

Fig. 5. A sample of multiple solutions at 0.1 g from Fig. 4: (a) 2D solution; (b) 3D solution.

gravity. Meanwhile, the bifurcation behavior can be studied by tracking solutions using the peak heater temperature T_p, which is similar to the heating power or the superheating, as the parameter. The bifurcation diagrams for zone length and surface temperature differences are illustrated in Figs. 6(a) and (b) respectively. Some field plots indicated in Fig. 6 are further illustrated in Fig. 7.

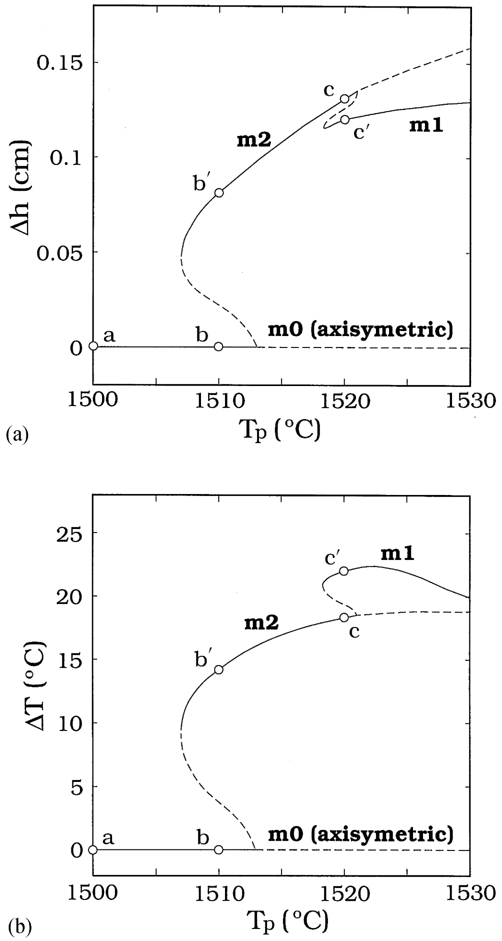

Fig. 6. Bifurcation diagrams of low superheating: (a) zone length deviation; (b) surface temperature deviation.

First, we start the solution at $T_p = 1500°C$, as shown in Figs. 6 and 7(a) (also Fig. 3(b)), the solution is axisymmetric and stable. Further increasing the heater temperature, again, we observe a subcritical bifurcation at about $T_p = 1513°C$. However, the new mode that bifurcates from the $m0$ mode is an $m2$ mode instead of an $m1$ mode. Two stable solutions b and b′ at $T_p = 1510°C$ are shown in Figs. 7(b) and (b′), respectively. The $m2$ mode b′ has a two-fold symmetry, which can be clearly seen from the cut of the isotherms at $z = L/2$. Therefore, two symmetric isotherms and flow fields can be obtained by cutting the zone properly. As shown at the bottom of Fig. 7(b′), although they are both symmetric with respect to the centerline, the results are quite different. By comparing the interface shapes from the two cuts, one may also get a 3D view of the interface shapes.

Further increasing the heater temperature, as shown in Fig. 6, we encounter a secondary bifurcation, and the $m2$ mode becomes unstable. The new mode branching from $m2$ is the $m1$ mode again. This bifurcation is subcritical as well. Two stable solutions c and c′ are further illustrated in Figs. 7(c) and (c′), respectively. As shown, because of the lower superheating, for the $m1$ mode, the deformation of the zone is much more significant than that with a higher superheating (e.g., Fig. 5(b)).

It is believed that the existence of the $m2$ mode at lower T_p is due to the much smaller aspect ratio of the molten zone. As the zone length is increased by increasing heating power, the $m1$ mode becomes dominant. Furthermore, the subcriticallity is due to the existence of the deformable interfaces. The bifurcation becomes supercritical if we fix the interfaces. Such an observation is similar to that in the two-phase Rayleigh Benard problems [12,13]. Again, although Ra_T^* is up to 5.78×10^5 ($\Delta T = 63.33°C$) for the $m1$ mode at $T_p = 1530°C$, the solution is still stable.

3.3. Dynamics due to heating and cooling

The subcritical nature discussed above is particularly important in practice. As one operates the system across the subcritical point or the turning point, a dramatic change of the solution may occur. Owing to the hystersis of the subcriticallity, the steady state of a set point is thus path dependent. To illustrate the significance of the bifurcation and multiple states, we also conduct time-dependent calculations for both heating and cooling situations. Again, the previous case with a lower superheating is used for illustration.

Fig. 8 shows the dynamic response of the heating by increasing T_p with a rate of 60°C/h from 1500°C to 1530°C. The bifurcation and turning points are indicated by the squares and asterisk, respectively. The time evolution of the zone length nonuniformity is shown in Fig. 8(a), and the temperature difference in Fig. 8(b). As shown, when the first bifurcation point is passed, the 3D flow starts to develop, but with some delay. Interestingly, multicell structures are found during the transition. For example, the six-fold cell at b is a typical transition for the solution from *m*0 to *m*2. After the transition, there is a dramatic change to *m*2. At $t = 30$ min, the flow is still *m*2, even though the secondary bifurcation has passed. Apparently, such a delay allows the *m*2 mode to appear and stay a bit longer before the final transition to the stable *m*1 mode. As shown, if we wait a bit longer, the *m*1 mode appears, and it is stable according to the stationary bifurcation diagram shown in Fig. 5(a). As compared with the transition from *m*0 to *m*2, the transition from *m*2 to *m*1 is less dramatic due to the smaller difference on the flow structure. However, since both transitions are subcritical, their transitions are not smooth at all. Particularly, there are some temperature fluctuations during transitions in Fig. 8(b). Parts of the fluctuations are due to the sampling error of the maximum temperature at the cell center of the zone surface, where no interpolation is used.

The dynamics for cooling, as shown in Fig. 9, are similar to that for heating, but the transition is much smoother. Still, as the turning point is passed, there is a dramatic change on the zone length and surface temperature differences. However, it should be pointed out that the final solution is path-dependent. For example, if we stop the final temperature at the region where two stable solutions exist, e.g., $T_\mathrm{p} = 1510°\mathrm{C}$, the final stable solution will be *m*0

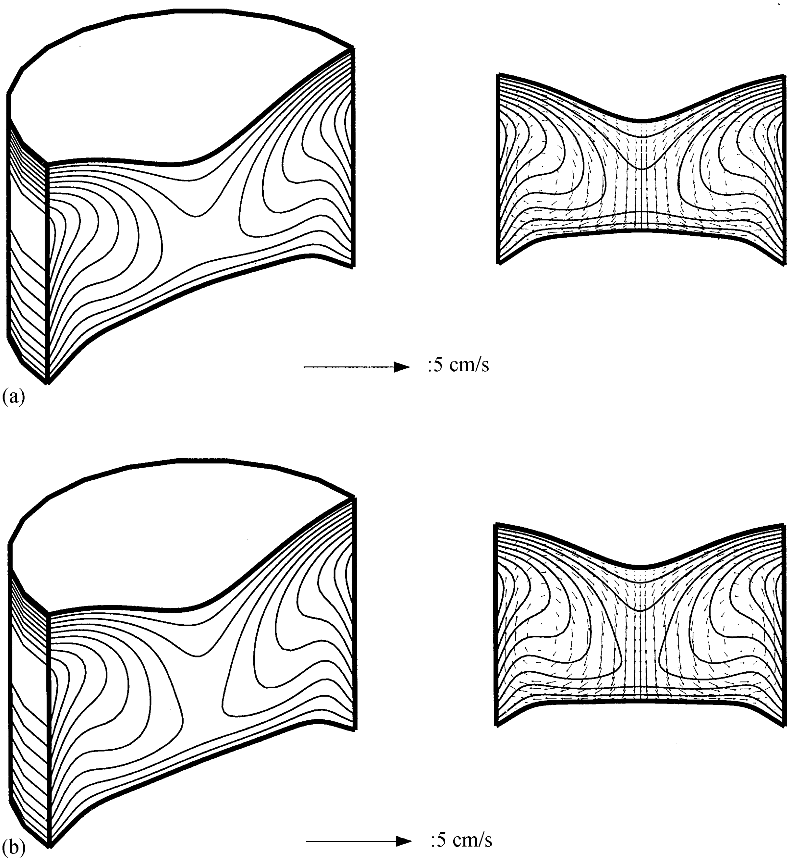

Fig. 7. Some solutions of Fig. 6: (a) 2D solution at $T_\mathrm{p} = 1500°\mathrm{C}$; (b) 2D solution at $T_\mathrm{p} = 1510°\mathrm{C}$; (b′) 3D *m*0 solution at $T_\mathrm{p} = 1510°\mathrm{C}$; (c) 3D *m*2 solution at $T_\mathrm{p} = 1520°\mathrm{C}$; (c′) 3D *m*1 solution at $T_\mathrm{p} = 1520°\mathrm{C}$.

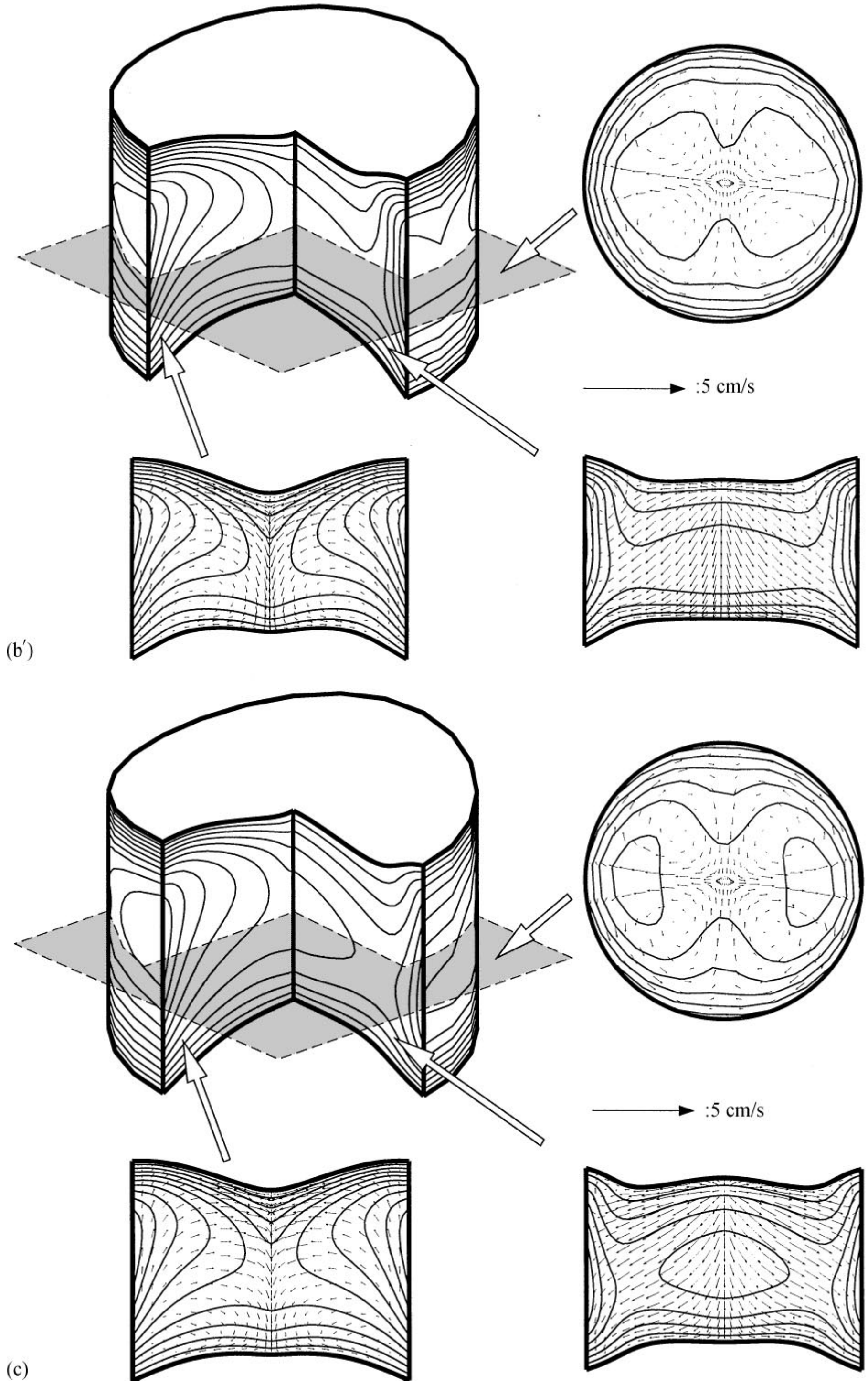

Fig. 7. (*continued*)

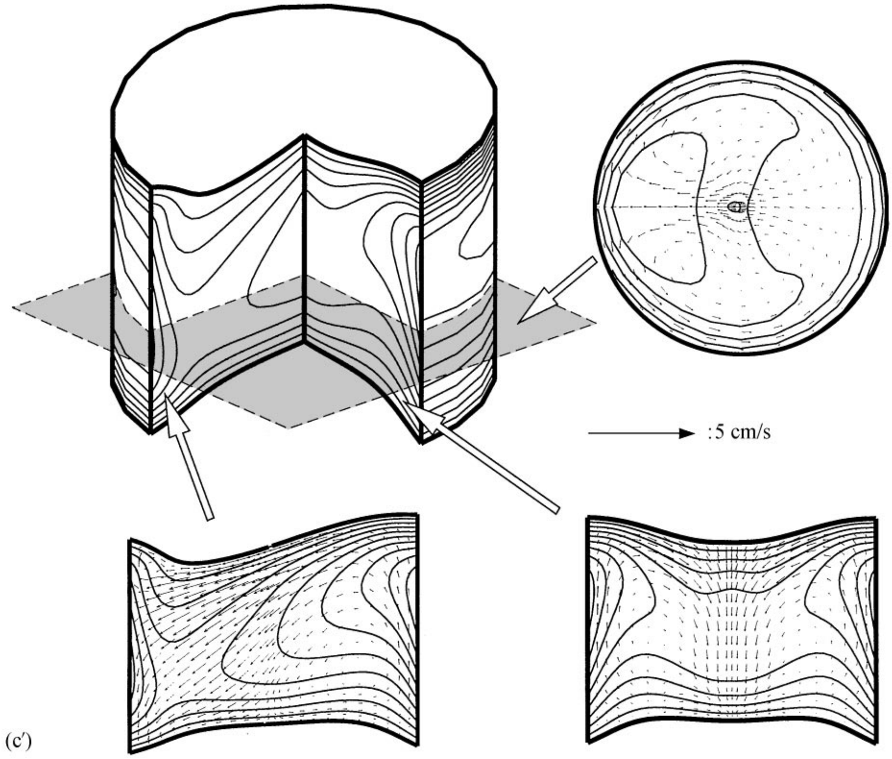

Fig. 7. (*continued*)

for heating (as a in Fig. 8) and $m2$ for cooling (as b in Fig. 9). In other words, different heating paths may lead to different steady solutions.

4. Conclusions

A three-dimensional time-dependent finite-volume method with front tracking for the moving interfaces is developed for VZM crystal growth. The nonlinear phenomena in VZM, including both symmetry breaking and multiple states, are investigated. With a higher superheating, the axisymmetric solution is not stable under normal gravity. To operate a stable axisymmetric mode, a lower superheating and a shorter zone are necessary. However, with the increasing superheating and zone length, the first symmetric breaking is subcritical and the branching mode has a two-fold symmetry at its midplane (an $m2$ mode). With the increasing superheating or zone length, the $m1$ mode can be obtained after the secondary subcritical bifurcation from the $m2$ mode. Between the turning point and the subcritical bifurcation point, there are two stable solutions. Unfortunately, detailed mechanisms leading to the nonlinear bifurcation are still not clear. As pointed out by Wanschura et al. [19], for low-Prandtl-number materials, the kinetic energy due to the inertial terms in the equation of motion predominates the flow stability. However, to further examine which term is dominant in the flow bifurcations, other numerical instruments, such as the energy method [19], need to be used.

The dynamic behavior of heating and cooling is further illustrated. As expected from the bifurcation diagrams, dramatic changes occur after passing the subcritical bifurcation point (for heating) or the limit point (for cooling). Even though there are some delay, the stationary bifurcation diagram still accurately predicts the final stable state. Furthermore, flow structures with multi-fold symmetry are

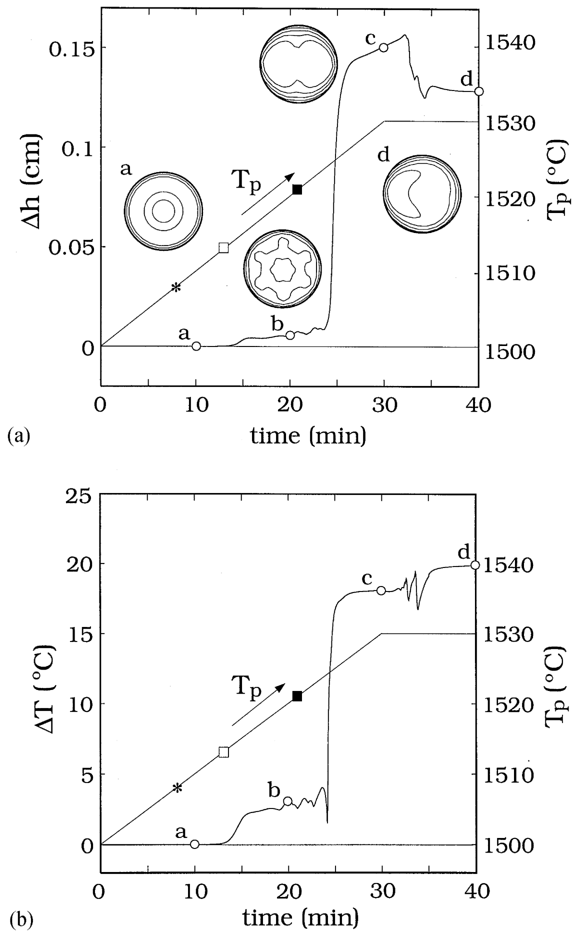

Fig. 8. Dynamic evolution of heating: (a) zone length deviation; (b) surface temperature deviation.

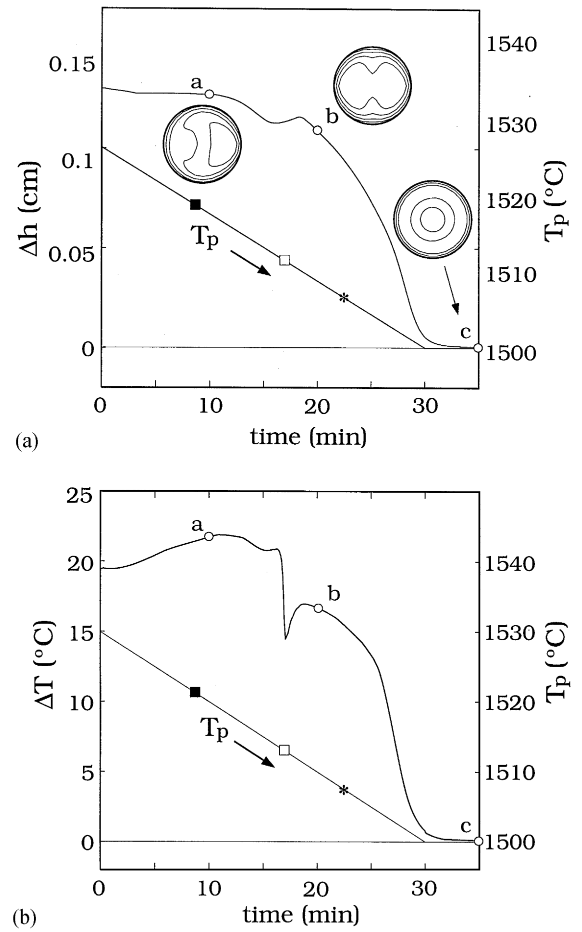

Fig. 9. Dynamic evolution of cooling: (a) zone length deviation; (b) surface temperature deviation.

also observed during the transition from the axisymmetric to *m*2 modes. The inherent unsteadiness, i.e., the Hopf bifurcation or the routes to chaos, though not discussed in detail here, is definitely an important subject that needs to be investigated in the future.

In summary, this study illustrates the significance of the natural symmetry breaking and multiple states that may be encountered in VZM crystal growth, even though the thermal environments are perfectly axisymmetric. The results presented here also help understand the possible uncertainty during growth or zone-refining experiments.

Acknowledgements

The authors are grateful for the support from the National Science Council and the National Center for High Performance Computing of the Republic of China under Grant No. NSC87-2214-E008-008.

References

[1] W.G. Pfann, Zone Melting, 2nd edition, Wiley, New York, 1966.
[2] E.S. Johnson, J. Crystal Growth 30 (1975) 249.

[3] L. Colombo, R.R. Chang, C.J. Chang, B.A. Baird, Vacuum Sci. Technol. A 6 (1988) 2795.
[4] R.L. Henry, P.E.R. Nordquist, R.J. Gorman, S.B. Qadri, J. Crystal Growth 109 (1991) 228.
[5] C.W. Lan, D.T. Yang, Numerical Heat Transfer, Part A 29 (1996) 131.
[6] C.W. Lan, D.T. Yang, Modeling Simul. Mater. Sci. Eng. 3 (1995) 71.
[7] C.W. Lan, M.C. Liang, J. Crystal Growth 186 (1998) 203.
[8] C.W. Lan, D.T. Yang, Int. Heat Mass Transfer 41 (1998) 4351.
[9] G. Muller, A. Ostrogorsky, in: D.T.J. Hurle (Ed.), Handbook of Crystal Growth 2b: Growth Mechanisms and Dynamics, North-Holland, Amsterdam, 1994, p. 754.
[10] G. Neumann, J. Fluid Mech. 24 (1990) 59.
[11] J. Baumgartl, W. Budweiser, G. Muller, G. Neumann, J. Crystal Growth 97 (1989) 9.
[12] S.H. Davis, U. Muller, D. Dietsche, J. Fluid Mech. 144 (1984) 133.
[13] C.W. Lan, M.C. Liang, M.K. Chen, Phys. Fluids 10 (1988) 1329.
[14] M.C. Liang, C.W. Lan, J. Comp. Phys. 127 (1996) 330.
[15] C.W. Lan, M.C. Liang, J. Comp. Phys. 152 (1999) 55.
[16] J.H. Ferziger, M. Peric, Computational Methods for Fluid Dynamics, Springer, New York, 1996.
[17] Fluent UNS 5.0 Usual Manual, Fluent Inc., 1999.
[18] C.W. Lan, C.H. Chian, J. Crystal Growth 203 (1999) 286.
[19] M. Wanschura, H.C. Kuhlmann, H.J. Rath, J. Fluid Mech. 326 (1996) 399.